

Charge-spin-coupled electrical transport properties in $\text{EuMoO}_3/\text{SrTiO}_3$ superlattices

T. C. Fujita, Y. Kozuka,^{*} H. Seki, and M. Kawasaki*Department of Applied Physics and Quantum-Phase Electronics Center (QPEC), University of Tokyo, Tokyo 113-8656, Japan*

(Received 29 December 2012; published 2 May 2013)

We investigate the structural and electrical properties of perovskite oxide superlattices composed of a ferromagnetic metal, EuMoO_3 , and a paramagnetic insulator, SrTiO_3 , grown on GdScO_3 (110) substrates by pulsed laser deposition. The results of x-ray diffraction show that the superlattices are formed as designed, while considerable interface roughening is recognized by high-resolution scanning transmission electron microscopy. In the transport properties, the temperature dependence of resistivity changes from metallic to insulating behaviors on reducing the thickness of EuMoO_3 . An anomalous Hall effect emerges in metallic superlattices, and its amplitude clearly corresponds to conductivity. Negative magnetoresistance is observed in all superlattices and is more pronounced in the insulating superlattices. These results indicate the existence of spin-canted and low-conductivity dead layers near the heterointerfaces due to the suppressed exchange coupling between electrons and local $\text{Eu } 4f^7$ spins.

DOI: [10.1103/PhysRevB.87.205402](https://doi.org/10.1103/PhysRevB.87.205402)

PACS number(s): 73.50.Bk, 73.21.Cd, 68.65.Cd, 75.47.Lx

I. INTRODUCTION

In the last a few decades, intensive efforts have been made to explore novel functionalities in heterostructures composed of transition-metal oxides, in which a number of fascinating physical properties has emerged as a result of strong electron correlations.^{1–4} Among them, heterojunctions and superlattices composed of magnetic perovskite oxides find intriguing properties that are superior to or unprecedented in conventional ferromagnets of elemental metals and their alloys. Most extensively studied compounds are a double-exchange ferromagnet of $(\text{La,Sr})\text{MnO}_3$ and an itinerant ferromagnet SrRuO_3 . For instance, an extremely large magnetoresistance was observed in $(\text{La,Sr})\text{MnO}_3/\text{SrTiO}_3/(\text{La,Sr})\text{MnO}_3$ tunneling junctions, making use of its fully spin-polarized half-metallic nature.⁵ As another example, ferromagnetic metal/antiferromagnetic insulator superlattices were fabricated as $(\text{La,Sr})\text{MnO}_3/(\text{La,Sr})\text{FeO}_3$, in which a keen competition between the two spin orders gave rise to a large spin fluctuation at the interfaces.⁶ These studies indicate that magnetic spin orders are modulated within only a few monolayers from the interfaces yet influence the magnetoelectrical properties in such heterostructures significantly. In this respect, investigating local properties at the interface is inevitable in designing functional heterojunction devices.

In order to assert these kinds of problems, frequently, ferromagnetic superlattices combined with a band insulator have been studied, since this structure enables us to clarify the effects of dimensionality and interfaces.^{7–9} In these studies, metal-insulator transitions and suppression of ferromagnetic ordering were examined by varying the thickness of the respective layers, revealing that the crossover occurs at a thickness characteristic of the magnetic material. In the case of $(\text{La,Sr})\text{MnO}_3/\text{SrTiO}_3$ superlattices, the ferromagnetic and metallic behaviors were found to be very fragile; they disappeared below the $(\text{La,Sr})\text{MnO}_3$ thickness of five unit cells.^{7,8} The origin was mainly attributed to electron transfer from $(\text{La,Sr})\text{MnO}_3$ to SrTiO_3 . This effect was shown to be the source of reduced tunneling magnetoresistance in the junctions.^{8,10} In the case of $\text{SrRuO}_3/\text{SrTiO}_3$ superlattices, in contrast, metallic behavior is quite robust and held down to

the SrRuO_3 thickness of two unit cells, although T_C reduced below four unit cells.⁹

In this work, we focus on EuMoO_3 , which we have recently synthesized as a new itinerant ferromagnet.¹¹ This compound does not exist in nature. However, the unusual valance combination of Mo^{4+} and Eu^{2+} is simultaneously stabilized in a form of epitaxial thin film. In contrast to aforementioned perovskite metallic ferromagnets, carrier transport and magnetism originate from different crystallographic sites; electrical conduction is driven at Mo^{4+} sites, while a large magnetic moment of $7 \mu_B$ /unit cell arises at Eu^{2+} sites. In this context, it is interesting to study charge transport together with the anomalous Hall effect (AHE) in the $\text{EuMoO}_3/\text{SrTiO}_3$ superlattices by controlling the thickness of each layer in order to investigate the effect of dimensionality and heterointerface on charge-spin coupling and to compare these properties with other magnetic oxide superlattices. We observed a clear metal-insulator transition increasing the EuMoO_3 layer thickness at around four monolayers. In metallic superlattices, AHE was observed. We ascribed the metal-insulator transition and disappearance of AHE to the existence of a “dead layer” near the interfaces where magnetic moments are not ordered, even below the T_C of bulk EuMoO_3 , and carrier transport is suppressed due to spin scattering. These results clearly suggest that the magnetism of EuMoO_3 is strongly correlated with carrier transport via hybridization between $\text{Mo } 4d$ and $\text{Eu } 4f$ orbitals.

II. EXPERIMENTAL

Epitaxial $[(\text{EuMoO}_3)_m/(\text{SrTiO}_3)_n]_{10}$ ($\text{EuMoO}_3/\text{SrTiO}_3 = m/n$) superlattices were grown on GdScO_3 (110) single-crystal substrates by pulsed laser deposition (PLD) using a KrF excimer laser ($\lambda = 248 \text{ nm}$). We fabricated two series of $\text{EuMoO}_3/\text{SrTiO}_3$ superlattices; in one series, thickness of EuMoO_3 was varied with a fixed SrTiO_3 thickness of five unit cells as $\text{EuMoO}_3/\text{SrTiO}_3 = m/5$ ($m = 1, 2, 4, 5$, and 10), while for the other series, the thickness of SrTiO_3 was varied with a fixed EuMoO_3 thickness of 10 unit cells as $\text{EuMoO}_3/\text{SrTiO}_3 = 10/n$ ($n = 1, 2, 3, 4, 5, 10$, and 20). We employed a commercial single crystal as a SrTiO_3 target and a polycrystalline phase-mixed ceramics target with a ratio

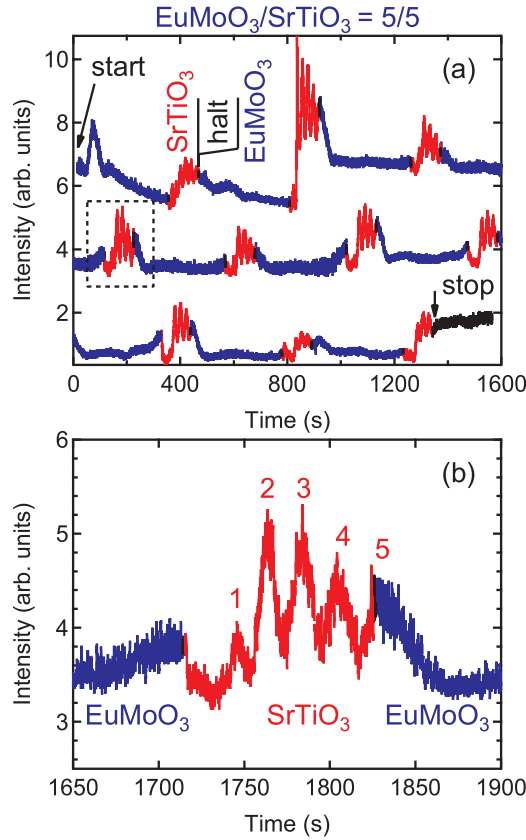


FIG. 1. (Color online) (a) RHEED intensity oscillations observed during the growth of a $\text{EuMoO}_3/\text{SrTiO}_3 = 10/5$ superlattice. Blue, red, and black parts represent the deposition of EuMoO_3 , SrTiO_3 , and the halt of deposition, respectively. (b) A magnified view of the intensity of RHEED oscillation is indicated by the dashed square in panel (a).

of $\text{Eu}/\text{Mo} = 1$ for EuMoO_3 . The films were deposited at a substrate temperature of 750°C under an atmosphere of 10 mTorr Ar gas containing 3% H_2 optimized for the growth of EuMoO_3 film.¹¹ The eximer laser fluence and frequency are $2 \text{ J}/\text{cm}^2$ and 5 Hz, respectively. The surface of the films was monitored *in situ* by reflection high-energy electron diffraction (RHEED). Although two-dimensional RHEED diffraction patterns were observed throughout deposition, RHEED intensity did not always oscillate, particularly for EuMoO_3 layers, as shown in Fig. 1. Thus, the thicknesses of both layers were controlled by the number of pulses using the deposition rates of each layer. When depositing the SrTiO_3 layer, in contrast, RHEED intensity usually oscillated, by which we could confirm deposition rate [Fig. 1(b)]. The film structures were characterized by a four-circle x-ray diffractometer (SmartLab, Rigaku Co.) and a scanning transmission electron microscope (STEM). We measured electrical properties using a liquid He cryostat equipped with a 9 T superconducting magnet (PPMS, Quantum Design Co.).

III. RESULTS AND DISCUSSIONS

A. Structural characterization

We first characterized the structures of the superlattices by x-ray diffraction (XRD). Figures 2(a) and 2(b) show 2θ - θ

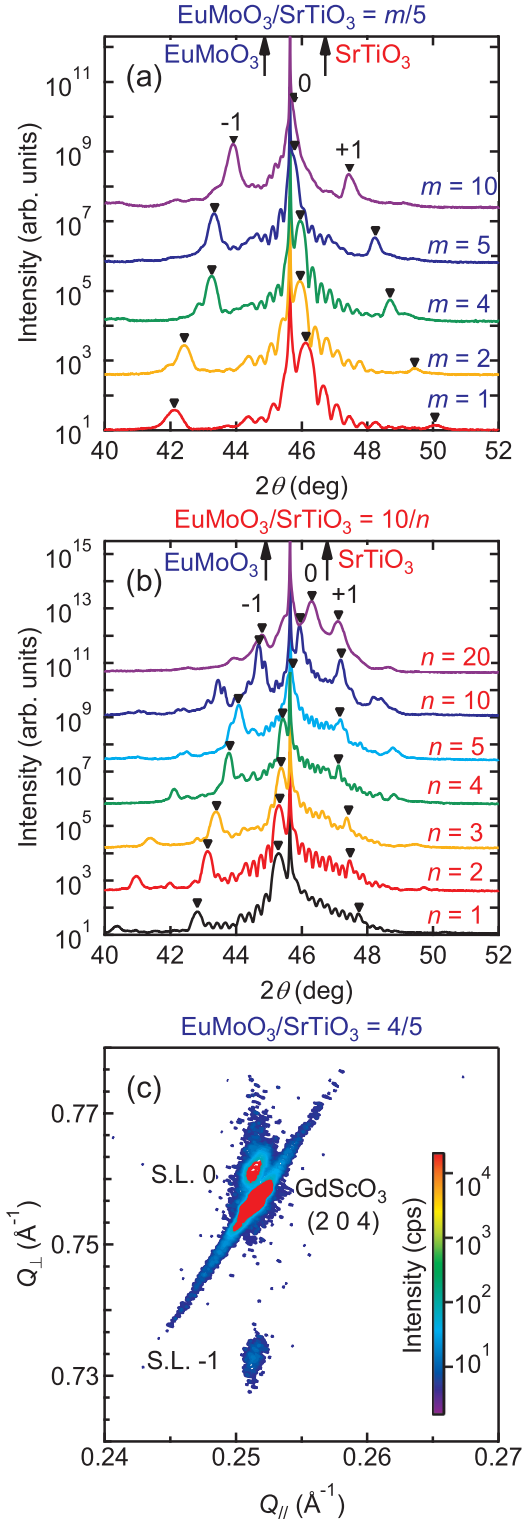


FIG. 2. (Color online) 2θ - θ XRD pattern around the GdScO_3 (220) peak for (a) $[(\text{EuMoO}_3)_m/(\text{SrTiO}_3)_5]_{10}$ ($\text{EuMoO}_3/\text{SrTiO}_3 = m/5$) and (b) $[(\text{EuMoO}_3)_{10}/(\text{SrTiO}_3)_n]_{10}$ ($\text{EuMoO}_3/\text{SrTiO}_3 = 10/n$). The curves are shifted vertically for clarity. The peak positions of individual EuMoO_3 and SrTiO_3 layers are represented by arrows. The fundamental and satellite peaks are also indicated by triangles, together with indices. (c) Reciprocal space mapping of XRD around the GdScO_3 (332) peak for an $\text{EuMoO}_3/\text{SrTiO}_3 = 4/5$. A fundamental peak and a satellite peak are denoted as S.L.0 and S.L.-1, respectively.

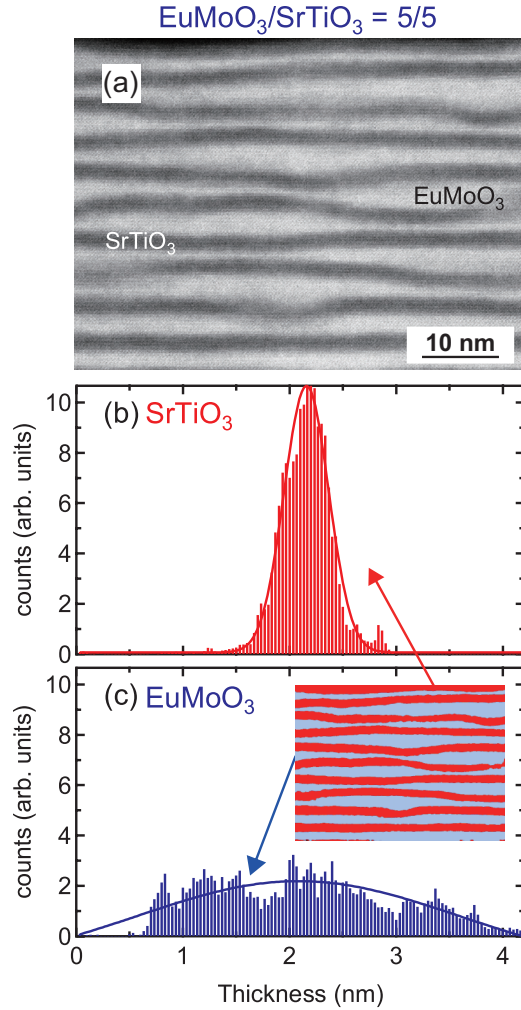


FIG. 3. (Color online) (a) A cross-sectional STEM image of a $\text{EuMoO}_3/\text{SrTiO}_3 = 5/5$. Dark and bright layers correspond to SrTiO_3 and EuMoO_3 , respectively. Thickness distribution histogram for (b) SrTiO_3 and (c) EuMoO_3 layers, where the thickness of each layer was quantified for a local horizontal position by counting vertically the number of pixels with this process repeated across the imaged range. The smoothed STEM image used for this analysis is shown in the inset of panel (c). The curves in panels (b) and (c) are the Gaussian fits to the data.

measurements around the GdScO_3 (220) peak for $\text{EuMoO}_3/\text{SrTiO}_3 = m/5$ and $\text{EuMoO}_3/\text{SrTiO}_3 = 10/n$, respectively. The fundamental superlattice peaks labeled 0 and the satellite superlattice peaks labeled ± 1 are clearly observed. The positions vary in accordance with the thickness ratio of EuMoO_3 to SrTiO_3 and the periodicity of the superlattices.¹² The in-plane relationship between the films and the substrate was investigated by reciprocal space mapping around GdScO_3 (332). Figure 2(c) shows a representative result for $\text{EuMoO}_3/\text{SrTiO}_3 = 4/5$, indicating coherently strained epitaxy of the film.

Complementary to XRD, a high-angle annular dark-field STEM image was observed for a superlattice of $\text{EuMoO}_3/\text{SrTiO}_3 = 5/5$, as shown in Fig. 3(a). The STEM image shows a significantly deformed interface structure from the design of the superlattice, although alternating stacks of

EuMoO_3 (bright) and SrTiO_3 (dark) layers are maintained. This unique structure is well clarified in the histogram of the thickness distribution of each layer, as shown in Figs. 3(b) and 3(c). For this analysis, the thickness of each layer was quantified for a local horizontal position by counting vertically the number of pixels in the smoothed STEM image shown in the inset of Fig. 3(c). This method was repeated across the imaged range. Gaussian fitting to the histograms was made to indicate that both layers have peak values at around 2 nm, which corresponds well to five layers of perovskite EuMoO_3 and SrTiO_3 unit cells. However, the thickness of the EuMoO_3 layer is more distributed than that of the SrTiO_3 layer due to the nonuniformity of the thickness. This structure can be considered characteristic of this material combination and may be understood based on the interface and surface energies, as thoroughly studied in semiconductor heterostructures.¹³ Generally, the epitaxial growth mode of material *A* on material *B* is explained based on the surface energies of materials *A* and *B* (σ_A and σ_B , respectively) and the interface energy between the two (σ_{AB}). In the case of $\sigma_B > \sigma_A + \sigma_{AB}$, *A* wets *B*, and two-dimensional growth (Frank–Van der Merwe growth) will occur. When $\sigma_B < \sigma_A + \sigma_{AB}$, *A* does not wet *B* and grows as islands (Volmer–Weber growth). For the superlattice with repeating units of *A/B/A/B*, one of the two must have a lower surface energy. As a consequence, if *A* is grown on *B* in two-dimensional growth mode, then *B* should be grown on *A* in three-dimensional growth mode with a thermodynamic limit.¹⁴ In reality, however, heterostructures are in a metastable state and seemingly regular superlattices are formed, making use of the nonequilibrium nature of thin-film growth. In our $\text{EuMoO}_3/\text{SrTiO}_3$ superlattice, SrTiO_3 layers are grown homogeneously, even on a deformed EuMoO_3 surface layer, probably because of the low surface energy of SrTiO_3 . Conversely, roughening of the EuMoO_3 layer may originate from higher surface energy and lower stability of the lattice than those of SrTiO_3 because EuMoO_3 is a nonequilibrium material in itself. The effect of epitaxial strain is not considered in this simple model, and coherent growth of the first EuMoO_3 layer from the substrate could be attributed to that. Although this explanation is plausible, details of the growth mechanism are not well understood at the moment, and further investigations are necessary.

In order to gain the overall feature of the superlattices, we compare the designed structures with experimentally determined structures by plotting periodicity ($t_{\text{SrTiO}_3} + t_{\text{EuMoO}_3}$) as a function of the intended one-layer thickness of EuMoO_3 (*m*) for $\text{EuMoO}_3/\text{SrTiO}_3 = m/5$ [Fig. 4(a)] and SrTiO_3 (*n*) for $\text{EuMoO}_3/\text{SrTiO}_3 = 10/n$ [Fig. 4(b)]. Here, we estimate $t_{\text{SrTiO}_3} + t_{\text{EuMoO}_3}$ from superlattice satellite peaks of XRD [Figs. 2(a) and 2(b)] and from the STEM image [Figs. 3(b) and 3(c)]. Despite the locally nonuniform structure seen by STEM, Figs. 4(a) and 4(b) certainly illustrate that the superlattices are grown as intended at a macroscopic scale. Below, we show the results of magnetotransport measurements as a macroscopic phenomenon in spite of severe roughening of the EuMoO_3 layers.

B. Electrical characterization

Next, we turn to the electrical properties of the superlattices. Figures 5(a) and 5(b) show the temperature dependence

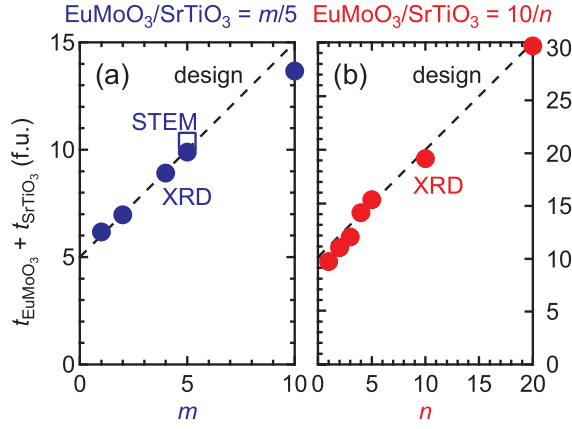


FIG. 4. (Color online) The periodicity ($t_{\text{SrTiO}_3} + t_{\text{EuMoO}_3}$) of superlattices estimated from XRD (circle) and STEM (square) as a function of intended one-period (a) EuMoO₃ thickness (m) for EuMoO₃/SrTiO₃ = $m/5$ and (b) SrTiO₃ thickness (n) for EuMoO₃/SrTiO₃ = $10/n$. The dashed lines represent the relations following the design.

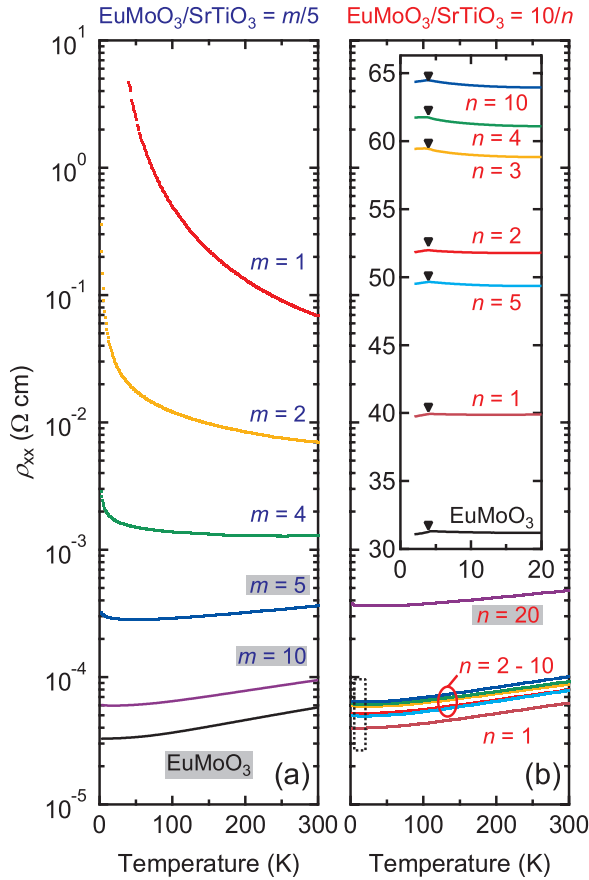


FIG. 5. (Color online) Temperature dependence of resistivity for (a) EuMoO₃/SrTiO₃ = $m/5$ and (b) EuMoO₃/SrTiO₃ = $10/n$. The data of a EuMoO₃ single-layer film are also plotted. The data of EuMoO₃/SrTiO₃ = $10/n$ ($n = 1-10$) from 2 K to 20 K are magnified in the inset of panel (b). Triangles represent temperatures where kink structures are observed, corresponding to the ferromagnetic transition of EuMoO₃. Representatives of samples with shaded labels are shown in Fig. 7.

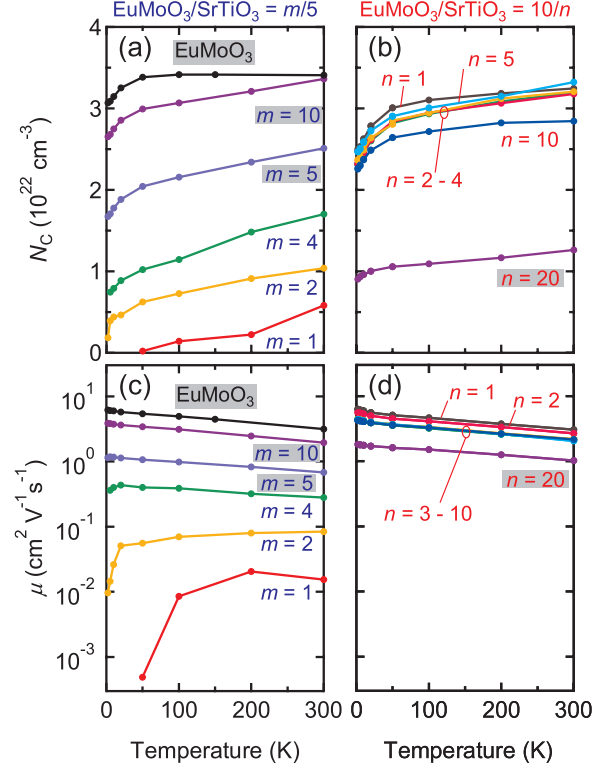


FIG. 6. (Color online) Temperature dependence of (a) carrier density N_C and (c) mobility μ for EuMoO₃/SrTiO₃ = $m/5$. The data of a EuMoO₃ single-layer film are also plotted. (b), (d) The same data set for EuMoO₃/SrTiO₃ = $10/n$. Representatives of samples with shaded labels are shown in Fig. 7.

of resistivity (ρ_{xx}) for EuMoO₃/SrTiO₃ = $m/5$ and $10/n$, respectively. Here, we assume that SrTiO₃ layers do not contribute to conduction and ρ_{xx} is calculated using the total thickness of EuMoO₃ layers. In fact, we confirmed that a thick SrTiO₃ film (~ 80 nm) grown under the same conditions showed large electrical resistivity (>100 $\Omega \cdot \text{cm}$) compared with an EuMoO₃ film. The resistivities of EuMoO₃/SrTiO₃ = $m/5$ ($m = 5, 10$) and EuMoO₃/SrTiO₃ = $10/n$ show metallic temperature dependence and approach the value close to that of a EuMoO₃ single-layer film on increasing the EuMoO₃ ratio with respect to SrTiO₃, which is additional evidence of negligible contribution of the SrTiO₃ layer to electrical conduction. The kink structures indicated by triangles in the inset of Fig. 5(b) should come from ferromagnetic transition of EuMoO₃. For EuMoO₃/SrTiO₃ = $m/5$ ($m = 1, 2, 4$), on the other hand, resistivities show insulating temperature dependence. These results imply the existence of a dead layer with thickness of approximately two unit cells from the interface between EuMoO₃ and SrTiO₃, where conductivity is much lower than that of the bulk part of the EuMoO₃ film.

In order to investigate crossover between insulating and metallic behaviors, we measured the Hall effect in the high-field region ($B > 5$ T) and estimated the carrier density (N_C) and mobility (μ), as shown in Figs. 6(a)–6(d). The carrier density monotonically decreases with decreasing temperature, probably due to localization, while mobility shows the obviously different temperature dependences between metallic and

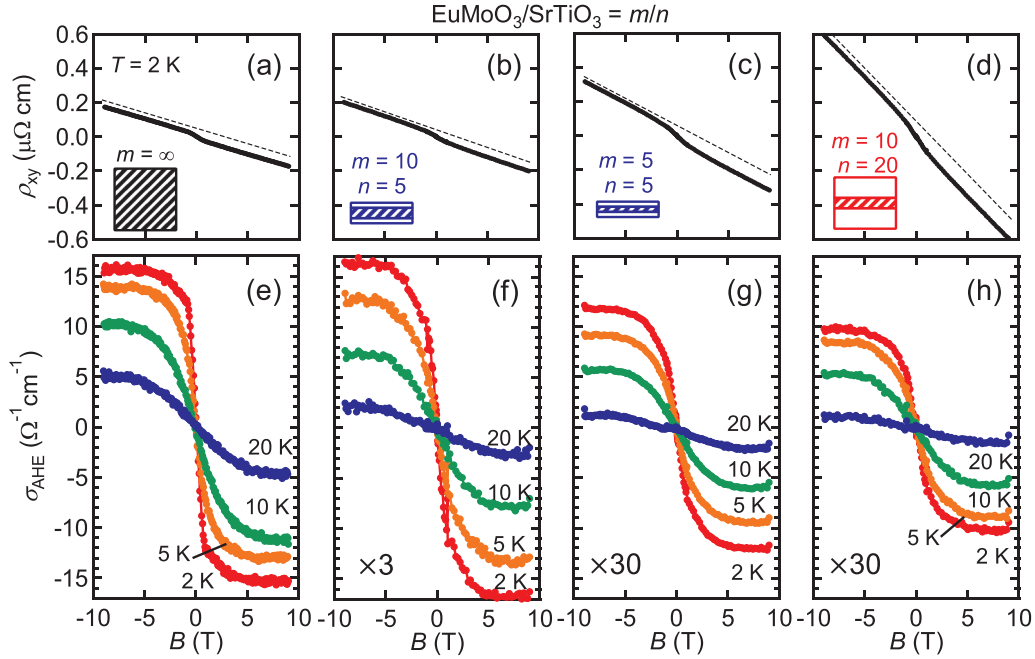


FIG. 7. (Color online) Magnetic field dependence of anomalous Hall resistivity ρ_{xy} of (a) EuMoO_3 single-layer film, (b) $\text{EuMoO}_3/\text{SrTiO}_3 = 10/5$, (c) $\text{EuMoO}_3/\text{SrTiO}_3 = 5/5$, and (d) $\text{EuMoO}_3/\text{SrTiO}_3 = 10/20$ at 2 K. Dashed lines indicate the ordinary Hall term. The insets schematically show the structure of films, where the open and hatched rectangles represent SrTiO_3 layers and EuMoO_3 layers, respectively. Black, blue, and red labels indicate the series of sample EuMoO_3 single-layer film, $\text{EuMoO}_3/\text{SrTiO}_3 = m/5$, and $\text{EuMoO}_3/\text{SrTiO}_3 = 10/n$, respectively. (e), (f) Magnetic field dependence of anomalous Hall conductivity σ_{AHE} for samples corresponding to panels (a)–(d) by varying the temperature from 20 K to 2 K. The data in panels (f)–(h) are magnified by the factors indicated in each panel.

insulating superlattices (i.e., increasing [decreasing] mobility with decreasing temperature for metallic [insulating] superlattices). $\text{EuMoO}_3/\text{SrTiO}_3 = 4/5$ shows weak temperature dependence in ρ_{xx} [Fig. 5(a)] and is considered to be located on a borderline between metallic and insulating phases. This metal-insulator crossover with decreasing EuMoO_3 thickness would be a result of weak localization when dimensionality is lowered.¹⁵ However, the exponential decrease in mobility at low temperature suggests that extrinsic effects, such as formation of an insulating dead layer or interface roughening, are more dominant than weak localization, which is characterized as a logarithmic temperature dependence of mobility.

To obtain magnetic properties, we measured AHE because the direct magnetization measurement is not feasible due to a large magnetic signal from the GdScO_3 substrate. As reported previously, magnetic property is reflected in AHE via an exchange interaction between Eu 4*f* spins and conducting electrons in Mo 5*d* bands.¹¹ Figures 7(a)–7(d) show the antisymmetrized data of Hall resistivity (ρ_{xy}) as a function of the magnetic field at 2 K for an EuMoO_3 single-layer film and representative superlattices ($\text{EuMoO}_3/\text{SrTiO}_3 = 10/5, 5/5, 10/20$). The Hall resistivity shows nonlinear magnetic field dependence near 0 T, suggesting AHE. Assuming the expression of $\rho_{xy} = \rho_0 B + \rho_{\text{AHE}}$ (ρ_0 is the ordinary Hall coefficient, and ρ_{AHE} is the anomalous Hall term), we subtract the linear ordinary Hall term in the high-field region [dashed line in Figs. 7(a)–7(d)] from ρ_{xy} and clarify the contribution of the anomalous term. The anomalous Hall conductivity shown in Figs. 7(e)–7(h) is

defined as^{16–18}

$$\sigma_{\text{AHE}} = -\frac{\rho_{\text{AHE}}}{\rho_{xx}^2 + \rho_{\text{AHE}}^2}. \quad (1)$$

Here, the vertical axes of Figs. 7(f)–7(h) are magnified by a factor given in each panel. By comparing the EuMoO_3 single-layer film [Fig. 7(e)] with the $\text{EuMoO}_3/\text{SrTiO}_3 = 10/5$ [Fig. 7(f)], the anomalous Hall conductivity is reduced by forming a superlattice. The AHE signal is further reduced by decreasing the thickness of the EuMoO_3 layers [Fig. 7(g)] or by increasing the thickness of the SrTiO_3 layers [Fig. 7(h)]. It is worth noting that the disappearance of AHE with decreasing EuMoO_3 thickness corresponds to the transition to an insulating phase, which demonstrates that ferromagnetism is mediated by conducting electrons.

Electric conduction and the magnetic property of the dead layer mentioned above is also elucidated based on the magnetoresistance ratio (MRR), $[\rho_{xx}(B) - \rho_{xx}(0 \text{ T})]/\rho_{xx}(0 \text{ T})$, at 2 K [Fig. 8(a)], which shows negative values in all of the samples, including the EuMoO_3 single-layer film. This can be understood by assuming Eu magnetic spins are canted in the dead layer to suppress electric conductivity with additional scattering. By applying a magnetic field, the spins are well aligned, which causes negative magnetoresistance.^{8,19,20} In $\text{EuMoO}_3/\text{SrTiO}_3 = 10/n$ and $\text{EuMoO}_3/\text{SrTiO}_3 = m/5$, with $m \geq 5$, MRR is small ($<6\%$) because most of the Eu spins in the conducting layers are spontaneously aligned without a magnetic field. In contrast, with decreasing m , the MRR increases up to 60% when $m = 2$ at 9 T, where the conducting layer is mostly composed of the dead layer with canted spins.

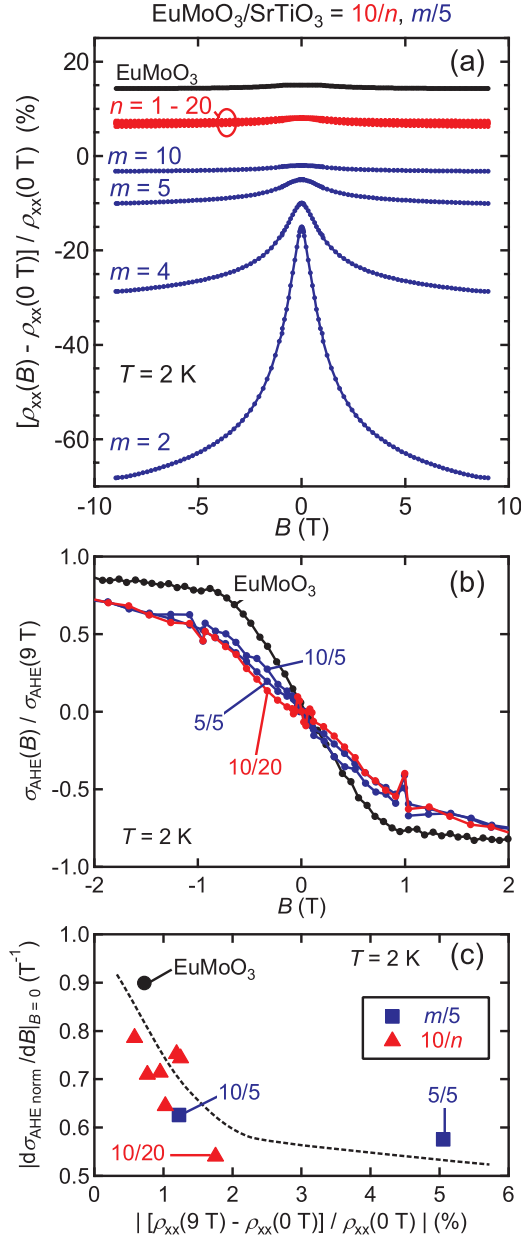


FIG. 8. (Color online) (a) Magnetic field dependence of MRR, $[\rho(B) - \rho(0 T)] / \rho(0 T)$ at 2 K for EuMoO₃/SrTiO₃ = $m/5$, EuMoO₃/SrTiO₃ = $10/n$, and a EuMoO₃ single-layer film. The data are shifted vertically for clarity. (b) Anomalous Hall conductivity at 2 K normalized by the value at 9 T $[\sigma_{AHE}(B) / \sigma_{AHE}(9 T)]$ of four representative samples shown in Fig. 7. (c) Absolute value of the initial slope of normalized σ_{AHE} - H curves at 2 K as a function of MRR for a EuMoO₃ single-layer film (circle), EuMoO₃/SrTiO₃ = $m/5$ (squares), and EuMoO₃/SrTiO₃ = $10/n$ (triangles).

The effect of canted spins at Eu sites in the dead layer is also evidenced by AHE. Figure 8(b) shows the magnetic field dependence of σ_{AHE} at 2 K normalized by the value at 9 T ($\sigma_{AHE, \text{norm}}$) for the four representative samples shown in Figs. 7(a)–7(d). Compared with that of a EuMoO₃ single-layer film, the low-field slopes of normalized σ_{AHE} - H curves are less sharp in superlattices, indicating that spontaneous magnetization of EuMoO₃ is diminished in the dead layer.

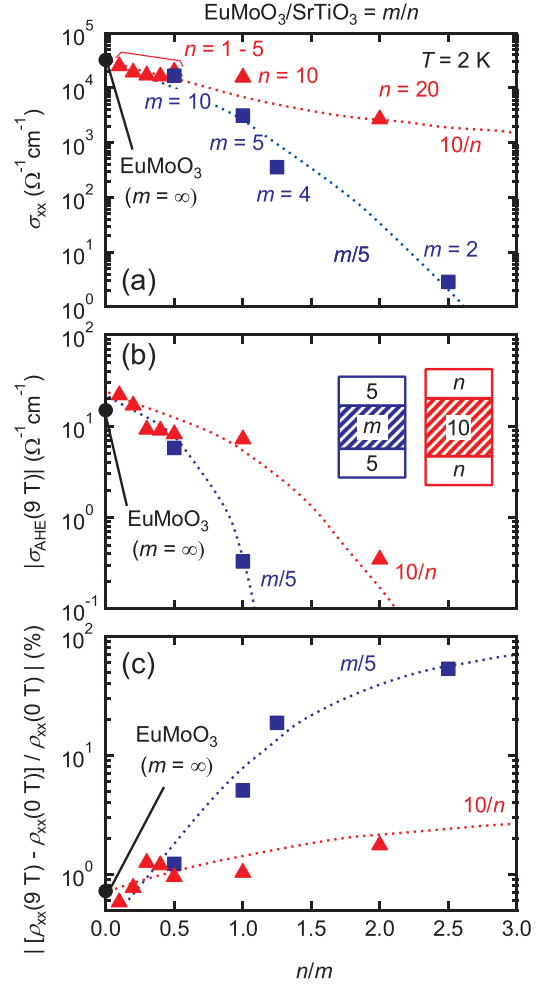


FIG. 9. (Color online) (a) Longitudinal conductivity, σ_{xx} ; (b) absolute values of anomalous Hall conductivity, $|\sigma_{AHE}(9 T)|$; and (c) absolute values of MRR (9 T) at 2 K as a function of n/m . Squares, triangles, and the circle represent data for EuMoO₃/SrTiO₃ = $m/5$, EuMoO₃/SrTiO₃ = $10/n$, and a EuMoO₃ single-layer film, respectively. Dashed curves are guides for the eye.

To summarize the effect of spin canting, the absolute value of the low-field slope $d\sigma_{AHE, \text{norm}}/dB$ at 0 T is plotted as a function of MRR at 9 T in Fig. 8(c), showing clear correlation between these two parameters.

Figures 9(a)–9(c) summarize the electrical properties of the superlattices, which show longitudinal conductivity, anomalous Hall conductivity, and MRR at 2 K, respectively, as a function of the SrTiO₃ ratio with respect to EuMoO₃ (n/m). In the EuMoO₃/SrTiO₃ = $m/5$ series, the longitudinal resistivity sharply decreases with decreasing EuMoO₃ thickness, m , accompanied by the reduction in anomalous Hall conductivity and an increase in MRR as a consequence of above-mentioned spin canting. In contrast, the EuMoO₃/SrTiO₃ = $10/n$ series shows a similar n/m dependence, but with higher σ_{xx} , particularly for large n/m , even at almost the same n/m . This suggests that longitudinal conductivity is dominated overall by the dead layer ratio in the conducting layer. Another interesting feature of the EuMoO₃/SrTiO₃ = $10/n$ series is the nontrivial reduction of conductivity and anomalous Hall

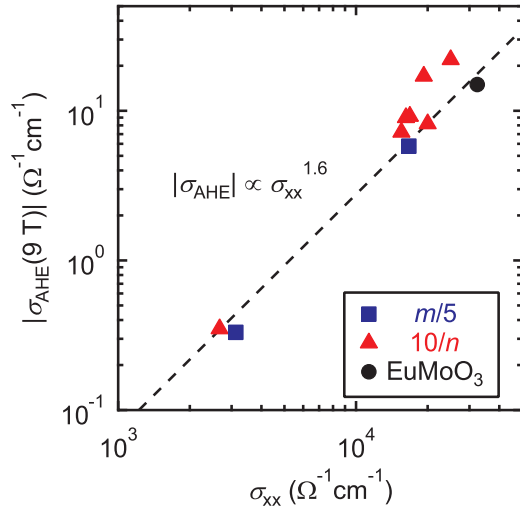


FIG. 10. (Color online) Relationship between absolute values of anomalous Hall conductivity ($|\sigma_{\text{AHE}}(9 \text{ T})|$) and longitudinal conductivity (σ_{xx}) at 2 K. Dashed line represents a scaling line expressed as $\sigma_{\text{AHE}} \sim \sigma_{xx}^{1.6}$.

conductivity when the SrTiO_3 layer is increased from $n = 10$ to 20. Since the total contribution of the dead layer would be considered the same in this series of superlattices, these reductions suggest that interlayer coupling also has a large effect via tunneling electrons. From a different viewpoint, anomalous Hall conductivity is well scaled by longitudinal conductivity in the form of $\sigma_{\text{AHE}} \propto \sigma_{xx}^{1.6}$, as reported previously for other ferromagnetic compounds (Fig. 10).^{16–18} Figure 11 schematically shows carrier transport and magnetic spin alignment in the superlattices based on the above discussion, where superlattice with a thick (thin) EuMoO_3 layer is less

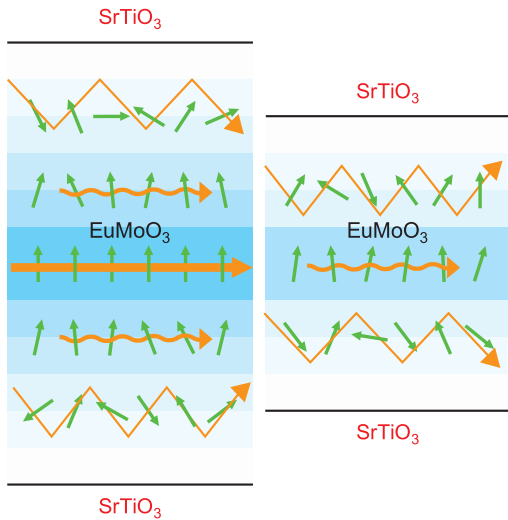


FIG. 11. (Color online) Schematic diagram of carrier transport in thick (left) and thin (right) EuMoO_3 layers with localized Eu^{2+} spins and itinerant Mo^{4+} electrons. The background color contrast visually represents conductivity, where the dark color represents a high-conductivity region and the light color represents a low-conductivity region.

(more) affected by dead layers and shows higher (lower) electric conductivity, which in turn results in magnetic ordering (disordering).

Now, we compare the transport properties of the $\text{EuMoO}_3/\text{SrTiO}_3$ superlattices with those of the $\text{SrRuO}_3/\text{SrTiO}_3$ (Ref. 9) and $(\text{La,Sr})\text{MnO}_3/\text{SrTiO}_3$ (Refs. 7 and 8) superlattices, which are representative oxide superlattices composed of metallic ferromagnet and insulating SrTiO_3 . In the case of the $\text{SrRuO}_3/\text{SrTiO}_3$ superlattice, metallic conductivity, together with ferromagnetism, was obtained down to a SrRuO_3 thickness of two unit cells. In contrast, more than five unit cells of $(\text{La,Sr})\text{MnO}_3$ are necessary to recover metallic conductivity in $(\text{La,Sr})\text{MnO}_3/\text{SrTiO}_3$ superlattices. This difference between them may be ascribed to the mechanism of magnetism and its coupling with electric conduction. SrRuO_3 is a metallic itinerant ferromagnet,²¹ and the metal-insulator crossover may be understood based on the loss of density of states in the thin limit.²² In contrast, the magnetism of $(\text{La,Sr})\text{MnO}_3$ is determined as a result of the competition between antiferromagnetic superexchange interaction and ferromagnetic double-exchange interaction,²⁰ causing relatively thick spin-canted layers at the interfaces with SrTiO_3 , where conductivity is significantly low, as the electric transport is strongly coupled with spin alignment. In this respect, $\text{EuMoO}_3/\text{SrTiO}_3$ is located in between, where metallic behavior arises above four unit cells of EuMoO_3 . Since the conducting electrons in $\text{Mo } 4d$ sites are weakly coupled with $\text{Eu } 4f$ spins via exchange coupling, the loss of magnetic alignment at the interfaces moderately lowers the electric conductivity.

IV. CONCLUSIONS

We have investigated the structural and electrical properties of $\text{EuMoO}_3/\text{SrTiO}_3$ superlattices, which we fabricated by pulsed laser deposition. While XRD showed that the superlattices were grown with the intended thicknesses and periodicity, STEM revealed deformed structure of the interface, possibly due to the local relaxation of the EuMoO_3 layer. As a consequence, the electrically dead layer with low conductivity exists a few monolayers from the interface, which results in carrier localization at low temperature. As the magnetism of EuMoO_3 is mediated by conducting carriers, the suppression of carrier transport causes the loss of magnetic order. In addition, we suggest that the interlayer coupling between EuMoO_3 layers through SrTiO_3 layers also can be an important factor in determining the electrical and magnetic properties of EuMoO_3 layers. Although we observed significant reduction of electrical conductivity at the thin limit, further improvement of superlattices may lead to novel quantum phenomena, given the large magnetic moment of Eu^{2+} and high electrical conductivity of Mo^{4+} (Ref. 23).

ACKNOWLEDGMENTS

We thank M. Ichikawa for helpful advice. This work was supported in part by JSPS Grant-in-Aid for Scientific Research(S) No. 24226002.

*Corresponding author: kozuka@ap.t.u-tokyo.ac.jp

- ¹Y. Tokura, *Phys. Today* **56**(7), 50 (2003).
- ²E. Dagotto and Y. Tokura, *MRS Bull.* **33**, 1037 (2008).
- ³P. Zubko, S. Gariglio, M. Gabay, P. Ghosez, and J.-M. Triscone, *Annu. Rev. Condens. Matter Phys.* **2**, 141 (2011).
- ⁴H. Y. Hwang, Y. Iwasa, M. Kawasaki, B. Keimer, N. Nagaosa, and Y. Tokura, *Nat. Mater.* **11**, 103 (2012).
- ⁵Y. Lu, X. W. Li, G. Q. Gong, G. Xiao, A. Gupta, P. Lecoeur, J. Z. Sun, Y. Y. Wang, and V. P. Dravid, *Phys. Rev. B* **54**, R8357 (1996).
- ⁶M. Izumi, Y. Murakami, Y. Konishi, T. Manako, M. Kawasaki, and Y. Tokura, *Phys. Rev. B* **60**, 1211 (1999).
- ⁷M. Izumi, Y. Ogimoto, Y. Okimoto, T. Manako, P. Ahmet, K. Nakajima, T. Chikyow, M. Kawasaki, and Y. Tokura, *Phys. Rev. B* **64**, 064429 (2001).
- ⁸M. Izumi, Y. Ogimoto, T. Manako, M. Kawasaki, and Y. Tokura, *J. Phys. Soc. Jpn.* **71**, 2621 (2002).
- ⁹M. Izumi, K. Nakazawa, and Y. Bando, *J. Phys. Soc. Jpn.* **67**, 651 (1998).
- ¹⁰F. Pailloux, D. Imhoff, T. Sikora, A. Barthélémy, J.-L. Maurice, J.-P. Contour, C. Colliex, and A. Fert, *Phys. Rev. B* **66**, 014417 (2002).
- ¹¹Y. Kozuka, H. Seki, T. C. Fujita, S. Chakraverty, K. Yoshimatsu, H. Kumigashira, M. Oshima, M. S. Bahramy, R. Arita, and M. Kawasaki, *Chem. Mater.* **24**, 3746 (2012).
- ¹²L. Vegard, *Z. Phys.* **5**, 17 (1921).
- ¹³Q. Xie, A. Madhukar, P. Chen, and N. P. Kobayashi, *Phys. Rev. Lett.* **75**, 2542 (1995).
- ¹⁴M. Copel, M. C. Reuter, Efthimios Kaxiras, and R. M. Tromp, *Phys. Rev. Lett.* **63**, 632 (1989).
- ¹⁵R. C. Dynes and P. A. Lee, *Science* **223**, 355 (1984).
- ¹⁶H. Toyosaki, T. Fukumura, Y. Yamada, K. Nakajima, T. Chikyow, T. Hasegawa, H. Koinuma, and M. Kawasaki, *Nat. Mater.* **3**, 221 (2004).
- ¹⁷T. Fukumura, H. Toyosakim, K. Ueno, M. Nakano, T. Yamasaki, and M. Kawasaki, *Jpn. J. Appl. Phys.* **46**, L642 (2007).
- ¹⁸N. Nagaosa, J. Sinova, A. H. MacDonald, and N. P. Ong, *Rev. Mod. Phys.* **82**, 1539 (2010).
- ¹⁹A. P. Ramirez, *J. Phys.: Condens. Matter* **9**, 8171 (1997).
- ²⁰A. Urushibara, Y. Moritomo, T. Arima, A. Asamitsu, G. Kido, and Y. Tokura, *Phys. Rev. B* **51**, 14103 (1995).
- ²¹L. Klein, J. S. Dodge, C. H. Ahn, G. J. Snyder, T. H. Geballe, M. R. Beasley, and A. Kapitulnik, *Phys. Rev. Lett.* **77**, 2774 (1996).
- ²²Y. J. Chang, C. H. Kim, S.-H. Phark, Y. S. Kim, J. Yu, and T. W. Noh, *Phys. Rev. Lett.* **103**, 057201 (2009).
- ²³M. Onoda and N. Nagaosa, *Phys. Rev. Lett.* **90**, 206601 (2003).